OPEN

Correspondence and
requests for materials
should be addressed to
J.S.C. (msecj@nus.
edu. sg)

Nanogranular TiN-ZrO$_2$ intermediate layer induced improvement of isolation and grain size of FePt thin films

K. F. Dong[1], H. H. Li[1], Y. G. Peng[2], G. Ju[2], G. M. Chow[1] & J. S. Chen[1]

[1]Department of Materials Science and Engineering, National University of Singapore, Singapore 117576, Singapore, [2]Seagate Technology, Fremont, CA 94538, USA.

The effects of TiN-ZrO$_2$ intermediate layer on the microstructures and magnetic properties of FePt films were investigated. The TiN-ZrO$_2$ intermediate layer was granular consisting of grains of solid solution of Ti(Zr)ON segregated by amorphous ZrO$_2$. By doping ZrO$_2$ into TiN intermediate layer, the FePt grains became better isolated from each other and the FePt grain size was reduced. For 20 vol. % ZrO$_2$ doping into TiN, the grain size decreased dramatically from 11. 2 nm to 6. 4 nm, and good perpendicular anisotropy was achieved simultaneously. For the FePt 4nm-SiO$_2$ 35 vol. % -C 20 vol. % films grown on top of the TiN-ZrO$_2$ 20 vol. % intermediate layer, well isolated FePt (001) granular films with coercivity higher than 18. 1 kOe and an average size as small as 6. 4 nm were achieved.

$L1_0$ ordered FePt alloy with high magnetocrystalline anisotropy ($K_u \sim 7 \times 10^7$ erg/cc) has been intensively investigated due to its potential application for ultra-high-density magnetic recording[1–2]. Great progress has been made in the fabrication of granular FePt thin films using MgO underlayer/intermediate layers[3–6]. However, small FePt grains grown on MgO showed large opening-up in the in-plane hysteresis loop due to the small surface energy of the MgO oxide intermediate layer, which caused non-wetting contact between FePt and MgO and led to the wide c-axis dispersion[7–9]. Recently, $L1_0$-FePt (001) films with high magnetic anisotropy and small opening-up of in-plane hysteresis loop were synthesized using conductive TiN intermediate layer that has a larger surface energy[10–12]. The conductive TiN intermediate can be fabricated by industry preferred direct-current sputtering. However, the FePt grains were not well isolated, which may cause undesirable large lateral exchange coupling and thus large transition noise.

In order to solve these problems, nanogranular TiN-ZrO$_2$ intermediate layer that is formed by doping ZrO$_2$ into TiN intermediate layer is proposed. It is known that the standard Gibb's energy of formation (-ΔG^0) at 300 K of ZrN (152 Kcal/gfw) is larger than that of TiN (145 Kcal/gfw), and (-ΔG^0) of ZrO$_2$ (248 Kcal/gfw) is larger than that of TiO (235 Kcal/gfw)[13]. Therefore, when ZrO$_2$ is doped into TiN intermediate layer, it is expected that ZrO$_2$ will remain stable and segregate from the TiN grains, thus forming the nanogranular TiN-ZrO$_2$ intermediate layer. Similar to the grain size and isolation control used in current perpendicular recording media[14], this nanogranular TiN-ZrO$_2$ intermediate layer is expected to be able to control the grain size and improve the grain isolation of FePt films. In this paper, the effects of TiN-ZrO$_2$ intermediate layer on the microstructure and magnetic properties of FePt films were investigated.

Results

Figure 1 shows XRD 2θ-scans of FePt (4 nm)-SiO$_2$ 35 vol. %-C 20 vol. %/TiN- ZrO$_2$/TiN/CrRu/glass with various ZrO$_2$ doping concentrations. All FePt films exhibited good $L1_0$ (001) texture. Only TiN (200) peak was observed and no peaks from any other TiN-ZrO$_2$ phases were found for all the samples, indicating a single fcc lattice structure. Meanwhile, with increasing ZrO$_2$ doping concentration, TiN (200) peak shifted towards a lower angle, suggesting the increase of the lattice constant a of TiN. Moreover, FePt (001) peak shifted to a higher angle with increasing ZrO$_2$ doping concentration from 0 vol. % to 20 vol. %. Further increasing ZrO$_2$ doping concentration to 30 vol. % caused the position of FePt (001) and (002) peak to a lower angle. As shown in Fig. 1(b), the lattice constant a_{TiN} increased from 4. 246Å to 4. 266Å, and c_{FePt} first decreased and then increased with increasing ZrO$_2$. The full width at half maximum (FWHM) of the rocking curve of the FePt (001) peak slightly increased from 5. 9 to 6. 9° as the ZrO$_2$ doping concentration increasing from 0 to 30 vol. %. The typical rocking curve of the FePt (001) peak with 30 vol. % ZrO$_2$ is shown in the inset of Fig. 1(b). The chemical ordering
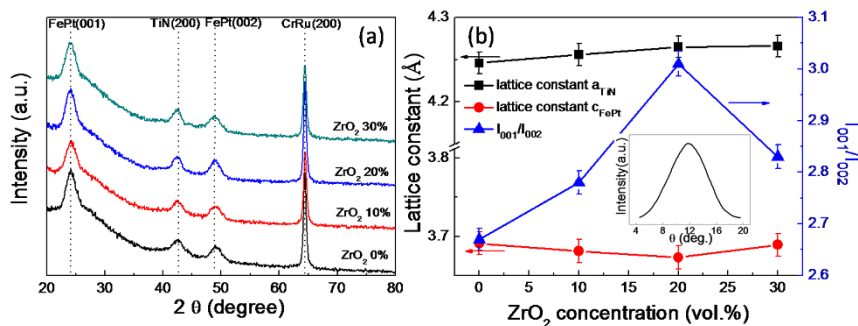
1

Figure 1 | (a) XRD spectra and (b) summaries of the lattice constant a_{TiN} and c_{FePt}, and integrated peak intensity ratio-I_{001}/I_{002} of FePt(4 nm)-SiO$_2$ 35 vol. %-C 20 vol. %/TiN-ZrO$_2$/TiN/CrRu/glass films with various ZrO$_2$ doping concentrations.

estimated by integrated peak intensity ratio I_{001}/I_{002} as shown in Fig. 1 (b), increased with increasing ZrO$_2$ concentration from 5 to 20 vol. % and then slightly decreased at 30 vol. % ZrO$_2$. The enhancement of the chemical ordering may be a result of the increased mismatch strain, which could assist the chemical ordering process. With high concentration ZrO$_2$, the lattice relaxation induced by the large misfit strain and the oxide interdiffusion may reduce the ordering parameter.

Figure 2 shows the planar view TEM images and cross-sectional TEM images of FePt (4 nm)-SiO$_2$ 35 vol. %-C 20 vol. %/TiN-ZrO$_2$/TiN/CrRu/glass films with various ZrO$_2$ doping concentrations. As seen from the planar view TEM images (Fig. 2a, b and c), by doping ZrO$_2$ into the TiN intermediate layer, the grain boundaries were more distinct. Moreover, grain size decreased from 11. 2 nm to 6. 4 nm for 20 vol. % ZrO$_2$ doping into TiN. Further increasing ZrO$_2$ concentration to 30 vol. % caused the increase of grain size to 7. 1 nm. The cross-sectional TEM images (Fig. 2 d, e and f) indicated that FePt-SiO$_2$-C films with a single-layer structure were grown on the top of TiN-ZrO$_2$ polycrystalline intermediate layer and FePt grains were well isolated. Moreover, FePt grains on TiN-ZrO$_2$ intermediate layer exhibited uniform square grain shape, indicating that the TiN-ZrO$_2$ possessed a moderate surface energy, which can achieve a good balance between epitaxial growth and island growth.

Figure 3 shows the M-H loops measured by SQUID of FePt (4 nm)-SiO$_2$ 35 vol. %-C 20 vol. %/TiN-ZrO$_2$/TiN/CrRu/glass films with various ZrO$_2$ doping concentrations. It can be seen that all the FePt samples shows good perpendicular anisotropy. With using TiN-ZrO$_2$ intermediate layer, the out-of-plane coercivity showed a slight increase (Fig. 3d), which was due to the increase of chemical ordering and the improvement of grain isolation. As for in-plane coercivity, it was increased as compared with pure TiN intermediate layer (Fig. 3d), which may be caused by the disturbance of the epitaxial growth of FePt by amorphous ZrO$_2$ in Ti(Zr)ON intermediate layer. Especially for the sample with 30 vol. % ZrO$_2$ doping, more amorphous ZrO$_2$ were formed, which resulted in deterioration of perpendicular anisotropy. Although, the perpendicular anisotropy showed slight deterioration, the 4nm-SiO$_2$ 35 vol. % -C 20 vol. % film grown on TiN/TiN-ZrO$_2$ 20 vol. % with a larger out-of-plane coercivity of 18. 1 kOe and a small in-plane coercivity of 2. 7 kOe was still realized.

Discussion

In order to understand the mechanism of the formation of smaller isolating grains grown on TiN-ZrO$_2$ intermediate layer TiN (5 nm)-(20 and 30 vol. %) ZrO$_2$/CrRu (30 nm)/glass films were also fabricated to investigate its chemical structure and microstructure e. g.
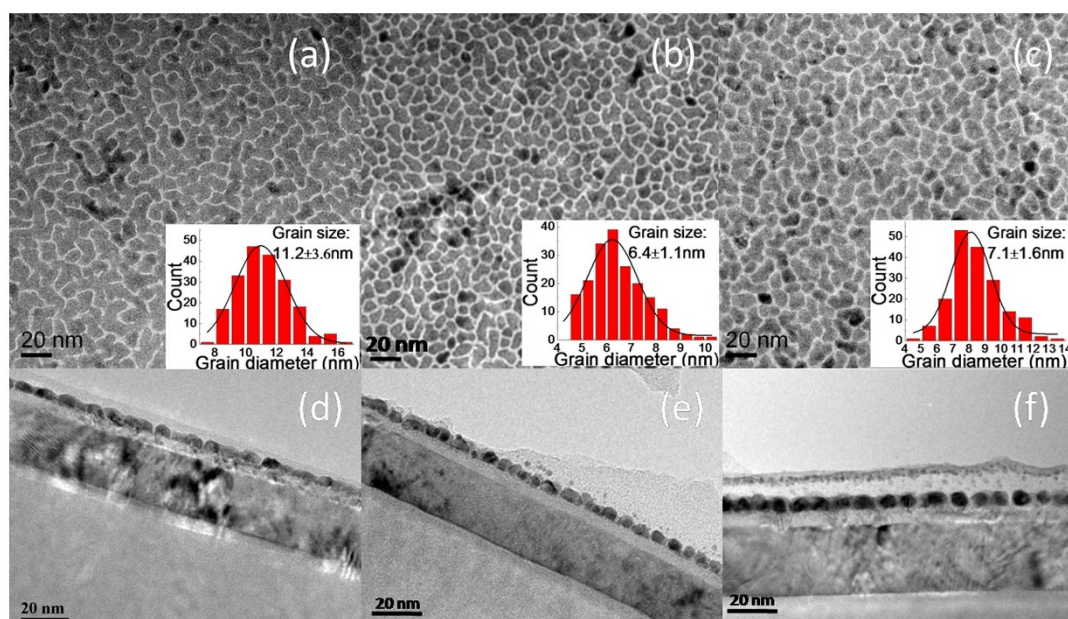

Figure 2 | Planar view TEM images (a, b, c) and cross-sectional TEM images (d, e, f) of FePt(4 nm)-SiO$_2$ 35 vol. %-C 20 vol. %/TiN-ZrO$_2$/TiN/CrRu/glass films with various ZrO$_2$ doping concentrations. The volume concentrations of ZrO$_2$ are: (a) and (d) 0%, (b) and (e) 20%, and (c) and (f) 30%. The insets are the corresponding grain size distribution.
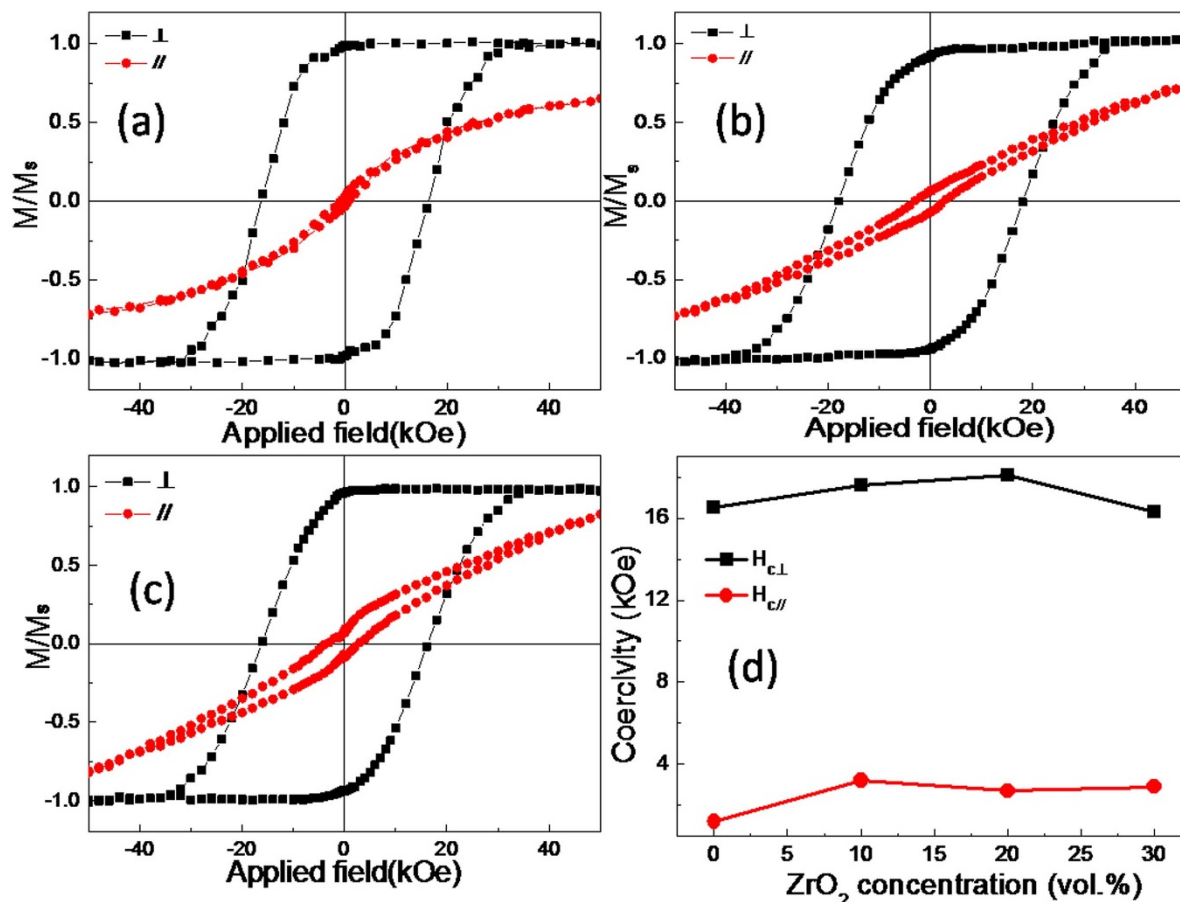
Figure 3 | M-H loops measured by SQUID of FePt(4 nm)-SiO$_2$ 35 vol. %-C 20 vol. %/TiN- ZrO$_2$/TiN/CrRu/glass films with various ZrO$_2$ doping concentrations. (a) 0 vol. %, (b) 20 vol. % and (c) 30 vol. %. (d) Summaries of out-of-plane and in-plane coercivities.
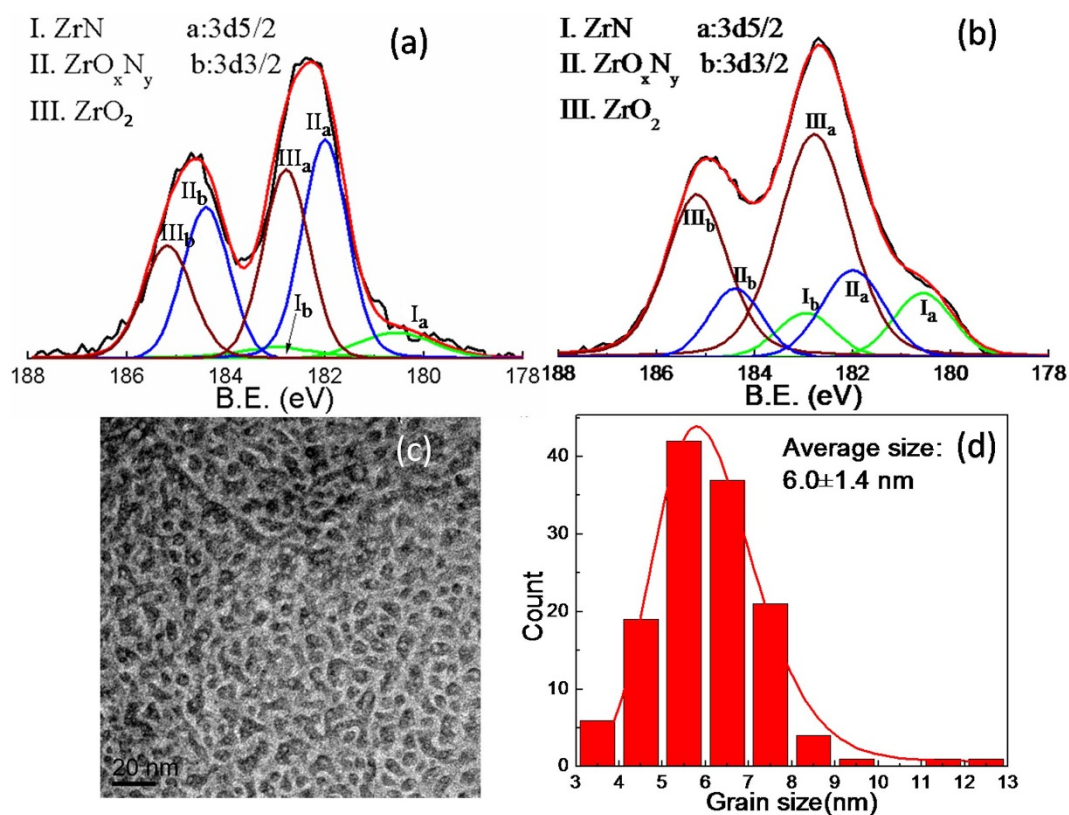

Figure 4 | XPS analysis of the Zr3d spectra of the TiN-ZrO$_2$ intermediate layer with (a) 20 vol. % and (b) 30 vol. % ZrO$_2$ doping, as well as planar view TEM images of CrRu(30 nm)/TiN(5 nm)-ZrO$_2$ 30 vol. % and (d) is the corresponding grain size distribution.
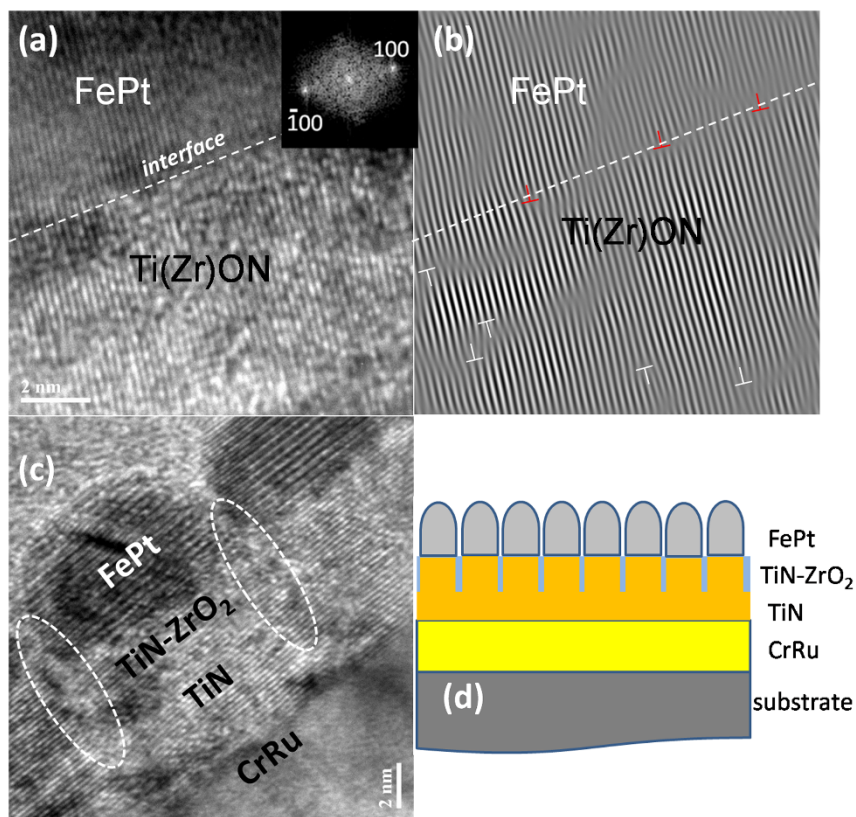
Figure 5 | (a) The enlarged high resolution TEM image of FePt(4 nm)-SiO$_2$ 35 vol. %-C 20 vol. %/TiN-30 vol. % ZrO$_2$/TiN/CrRu/glass film observed from zone axis <010>, as indicated by the inset diffraction patterns; (b) is the corresponding inverse fast Fourier transform (iFFT) images. The dislocations are labeled by (⊥) and interfacial dislocations are with red color. (c) the high resolution TEM images of FePt(4 nm)-SiO$_2$ 35 vol. %-C 20 vol. %/TiN-30 vol. % ZrO$_2$/TiN/CrRu/glass fim (white elliptical line roughly shows the grain boundary regions), (d) the illusration drawing of the layer structure.

whether it formed a nanocomposite (mixture of TiN phase and ZrO$_2$ phase) or a solid solution of Ti(Zr)ON. The chemical compositions of the Zr element in the TiN-ZrO$_2$ intermediate layer for these films were examined by high resolution XPS. Fig. 4 (a) and (b) show the Zr3d spectra of the samples with 20 vol. % and 30 vol. % ZrO$_2$, respectively. Peak positions and their assignments are based on a method reported previously[15–19]. As expected, the Zr element in TiN-ZrO$_2$ layer existed in three chemical forms: ZrN, ZrO$_x$N$_y$ and ZrO$_2$. The molar ratio of ZrN, ZrO$_x$N$_y$ and ZrO$_2$ were 9. 3%, 49. 0% and 41. 7% for 20 vol. % ZrO$_2$ doping, and 14. 4%, 20. 8% and 64. 8% for 30 vol. % ZrO$_2$ doping. This indicated that the both Ti(Zr)ON solid solution grains and amorphous ZrO$_2$ were formed simultaneously and thus the granular TiN-ZrO$_2$ was formed. Furthermore, the full width at half maximum (FWHM) of the rocking curve of the TiN (200) peak slightly increased from 5. 2 to 6. 1° as the ZrO$_2$ doping concentration increasing from 0 to 30 vol. % (the results are not shown here). Combined with the XRD results in Fig. 1, the solid solution Ti(Zr)ON is fcc (200) texture and therefore by using ZrO$_2$ doping the texture of TiN would not be deteriorated obviously. Moreover, fcc ZrN content increased greatly with increasing ZrO$_2$, leading to an increase of the misfit strain and the decrease of FePt lattice constant c, because the lattice constant of ZrN (4. 574Å) is larger than that of TiN (4. 238Å). Planar view TEM of the TiN-ZrO$_2$ 30 vol. %/CrRu/glass film was carried out to further prove the forming of granular TiN-ZrO$_2$, and the results are shown in Fig. 4(c). It can be seen that the TiN-ZrO$_2$ 30 vol. % films was granular. It exhibited small grains with an average grain size of around 6 nm (Fig. 4d). The well isolated Ti(Zr)ON grains suggested that the amorphous ZrO$_2$ content (64. 8 at. %) remained in grain boundaries.

Figure 5(a) shows the enlarged high resolution TEM image of FePt (4 nm)-SiO$_2$ 35 vol. %-C 20 vol. %/TiN-30 vol. % ZrO$_2$/TiN/CrRu/ glass observed from zone axis <010>, as indicated by the inset diffraction patterns, and Fig. 5 (b) is the corresponding inverse fast Fourier transform (iFFT) images. The dislocations are labeled by (⊥) and interfacial dislocations are with red color. It shows the matching of the atomic planes across the FePt and Ti(Zr)ON interface from the HR-TEM images. The interface was sharp and clear. The SAED patterns spots of FePt and Ti(Zr)ON were overlapped, implying a good epitaxial growth of FePt on Ti(Zr)ON. The epitaxial relationship Ti(Zr)ON (002) <200>//FePt (001) <100> was confirmed. From the iFFT images, the dislocations (Fig. 5b) can be clearly seen, which may be caused by diffusion of the amorphous ZrO$_2$. Moreover, the misfit dislocations (red color in Fig 5b) were found at Ti(Zr)ON/FePt interfaces. It is known that the interfacial dislocations can reduce mismatch strain and improve epitaxial growth. From the high resolution TEM images of the FePt-SiO$_2$-C film grown on TiN-30 vol. % ZrO$_2$ intermediate layer (Fig. 5c), the granular structure of TiN-ZrO$_2$ intermediate layer was observed. The grain boundaries with discontinuous lattice plane can be found in the region encircled by white dash line in Fig. 5(c). Additionally, the FePt grain size matched very well with TiN-ZrO$_2$ grain size. It indicated that FePt followed the epitaxial growth of the Ti(Zr)ON grain during deposition, which can be illustrated by the schematic drawing in the Fig. 5(d). The ZrO$_2$ doping in TiN led to the formation of Ti(Zr)ON solid solution grains and amorphous ZrO$_2$ segregation simultaneously. Thereafter, the FePt grains were formed epitaxially on top of Ti(Zr)ON grains.

Methods

target and a ZrO_2 target by changing ZrO_2 sputtering power. The FePt-SiO_2-C films were co-sputtered from a FePt target, a SiO_2 target and a C target. The FePt and C targets were used DC powers, and the SiO_2 target was used RF power. The sputtering rate for FePt, SiO_2 and C were 1. 6 nm/min, 0. 86 nm/min and 0. 61 nm/min, respectively. The volume concentration for SiO_2 and C were fixed at 35 vol. % and 20 vol. %, respectively. The deposition temperatures of CrRu, TiN-ZrO_2 and FePt were 280, 480 and 480°C, respectively. During the sputtering process, FePt films were epitaxial grown on TiN-ZrO_2 intermediate layer and $L1_0$ ordered FePt films with (001) texture were formed. Moreover, the SiO_2 and C were diffused into the grain boundary of FePt grains, and isolated the FePt grains, thus the $L1_0$-FePt nanoparticles were formed.

Characterization of FePt films. The elemental compositions and chemical states of TiN-ZrO_2 intermediate layers were determined by x-ray photoelectron spectroscopy (XPS). Crystallographic structure and microstructures of the samples were measured by x-ray diffraction (XRD) and transmission electron microscopy (TEM). Magnetic properties were characterized at room temperature by a superconducting quantum interference device (SQUID) with a maximum applied field of 6 Tesla.

1. Weller, D., Mosendz, O., Parker, G., Pisana, S. & Santos, T. S. $L1_0$ FePtX–Y media for heat-assisted magnetic recording. *Phys. Status Solidi A* **210**, 1245–1260 (2013).
2. Wu, X. W., Guslienko, K. Y., Chantrell, R. W. & Weller, D. Magnetic anisotropy and thermal stability study on FePt nanoparticle assembly. *Appl. Phys. Lett.* **82**, 3475–3477 (2003).
3. Yan, M. L. *et al.* Fabrication of nonepitaxially grown double-layered FePt:C/ FeCoNi thin films for perpendicular recording. *Appl. Phys. Lett.* **83**, 3332–3334 (2003).
4. Wu, Y. C., Wang, L. W. & Lai, C. H. Low-temperature ordering of (001) granular FePt films by inserting ultrathin SiO_2 layers. *Appl. Phys. Lett.* **91**, 072502-1–072502-3 (2007).
5. Li, H. H. *et al.* Highly (001)-Textured $L1_0$ FePt-SiO_2-C Films with Well-Isolated Small Grains Using TiON Intermediate Layer. *Appl. Phys. Express.* **6**, 075502–075505 (2013).
6. Ding, Y. F., Chen, J. S., Lim, B. C., Hu, J. F. & Ju, G. Granular $L1_0$ FePt: TiO_2 (001) nanocomposite thin films with 5 nm grains for high density magnetic recording. *Appl. Phys. Lett.* **93**, 032506-1–032506-3 (2008).
7. Chen, J. S. *et al.* Low temperature deposited $L1_0$ FePt-C (001) films with high coercivity and small grain size. *Appl. Phys. Lett.* **91**, 132506-1–132506-3 (2007).
8. Yang, E., Ratanaphan, S., Zhu, J. G. & Laughlin, D. E. Structure and magnetic properties of $L1_0$-FePt thin films on TiN/RuAl underlayers. *J. Appl. Phys.* **109**, 07B770-1–07B770-3 (2011).
9. Zhang, L., Takahashi, Y. K., Perumal, A. & Hono, K. $L1_0$-ordered high coercivity (FePt)Ag–C granular thin films for perpendicular recording. *J. Magn. Magn. Mater.* **322**, 2658–2664 (2010).
10. Dong, K. F. *et al.* Well-isolated $L1_0$ FePt–SiN_x–C nanocomposite films with large coercivity and small grain size. *J. Appl. Phys.* **111**, 07A308-1–07A308-3 (2012).
11. Dong, K. F. *et al.* Nanocomposite $L1_0$ FePt-SiN_x and FePt-SiN_x-C films with large coercivity and small grain size on a TiN intermediate layer. *J. Magn. Magn. Mater.* **324**, 2637–2644 (2012).
12. Dong, K. F. *et al.* Control of microstructure and magnetic properties of FePt films With TiN intermediate layer. *IEEE Trans. Magn.* **49**, 668–674 (2013).
13. Reed, T. B. *Free energy of formation of binary compounds* (MIT, Cambridge, MA, 1971).
14. Piramanayagam, S. N. Perpendicular recording media for hard disk drives. *J. Appl. Phys.* **102**, 011301-1–011301-22 (2007).
15. Vaz, F. *et al.* Property change in ZrN_xO_y thin films: effect of the oxygen fraction and bias voltage. *Thin Solid Films* **469**, 11–17 (2004).
16. Arias, D. F., Arango,Y. C. & Devia, A. Study of TiN and ZrN thin films grown by cathodic arc technique. *Appl. Surf. Sci.* **253**, 1683–1690 (2006).
17. Martin, P. J., Bendavid, A., Cairney, J. M. & Hoffman, M. Nanocomposite Ti-Si-N, Zr-Si-N, Ti-Al-Si-N, Ti-Al-V-Si-N thin film coatings deposited by vacuum arc deposition. *Surf. Coat. Technol.* **200**, 2228–2235 (2005).
18. Huang, J. H., Chang, K. H. & Yu, G. P. Synthesis and characterization of nanocrystalline ZrN_xO_y thin films on Si by ion plating. *Surf. Coat. Technol.* **201**, 6404–6413 (2007).
19. Craciun, D. *et al.* Characteristics of ZrC/ZrN and ZrC/TiN multilayers grown by pulsed laser deposition. *Appl. Surf. Sci.* **257**, 5332–5336 (2011).

Acknowledgments

Author contributions

K.F.D., H.H.L. and J.S.C. were involved in the design of experiments. K.F.D., H.H.L. and J.S.C. performed the experiments and analyzed results. K.F.D., H.H.L. and J.S.C. wrote the manuscript. J.S.C. supervised the project. Y.G.P., G.J. and G.M.C. discussed the results and commented on the manuscript.

Additional information